Chemical Science

ROYAL SOCIETY OF CHEMISTRY

EDGE ARTICLE

View Article Online
View Journal | View Issue

Cite this: *Chem. Sci.*, 2024, **15**, 11856

All publication charges for this article have been paid for by the Royal Society of Chemistry

Internal strain-driven bond manipulation and band engineering in $Bi_{2-x}Sb_xYO_4Cl$ photocatalysts with triple fluorite layers†

Artem Gabov,[ab] Daichi Kato, *[a] Hiroki Ubukata, [a] Ryotaro Aso,[c] Naoji Kakudou,[a] Koji Fujita, [d] Hajime Suzuki, [a] Osamu Tomita, [a] Akinori Saeki, [e] Ryu Abe, [a] Smagul Zh Karazhanov*[f] and Hiroshi Kageyama *[a]

In extended solid-state materials, the manipulation of chemical bonds through redox reactions often leads to the emergence of interesting properties, such as unconventional superconductivity, which can be achieved by adjusting the Fermi level through, *e.g.*, intercalation and pressure. Here, we demonstrate that the internal 'biaxial strain' in tri-layered fluorite oxychloride photocatalysts can regulate bond formation and cleavage without redox processes. We achieve this by synthesizing the isovalent solid solution $Bi_{2-x}Sb_xYO_4Cl$, which undergoes a structural phase transition from the ideal Bi_2YO_4Cl structure to the Sb_2YO_4Cl structure with $(Bi,Sb)_4O_8$ rings. Initially, substitution of smaller Sb induces expected lattice contraction, but further substitution beyond $x > 0.6$ triggers an unusual lattice expansion before the phase transition at $x = 1.5$. Detailed analysis reveals structural instability at high x values, characterized by Sb–O underbonding, which is attributed to tensile strain exerted from the inner Y sublayer to the outer (Bi,Sb)O sublayer within the triple fluorite block – a concept well-recognized in thin film studies. This concept also explains the formation of zigzag Bi–O chains in Bi_2MO_4Cl (M = Bi, La). The Sb substitution in $Bi_{2-x}Sb_xYO_4Cl$ elevates the valence band maximum, resulting in a minimized bandgap of 2.1 eV around $x = 0.6$, which is significantly smaller than those typically observed in oxychlorides, allowing the absorption of a wider range of light wavelengths. Given the predominance of materials with a double fluorite layer in previous studies, our findings highlight the potential of compounds endowed with triple or thicker fluorite layers as a novel platform for band engineering that utilizes biaxial strain from the inner layer(s) to finely control their electronic structures.

Received 29th March 2024
Accepted 7th June 2024

DOI: 10.1039/d4sc02092h

rsc.li/chemical-science

Introduction

In photocatalysis, precise control of both the valence band maximum (VBM) and the conduction band minimum (CBM) is critical. Mixed-anion compounds, such as oxynitrides, are well-suited for enabling a response to visible light.[1–4] For example, in BiOX oxyhalides (X = Cl, Br, I),[1] the halogen p orbitals reside above the O-2p orbitals, elevating the VBM in the sequence of decreasing electronegativity. Recently, structurally related Sillén and Sillén-Aurivillius layered oxyhalides with double fluorite layers, such as $PbBiO_2X$[5] and Bi_4NbO_8X (X = Cl, Br), have emerged as promising photocatalysts for water splitting under visible light irradiation, due to their outstanding stability against self-oxidation by photogenerated holes.[6,7] This stability arises from the formation of VBM composed primarily of the O-2p orbitals, unlike in BiOX. The high energy levels of the O-2p orbitals stem from the lone pair interaction between the Bi-6s and O-2p orbitals,[8] coupled with electrostatic repulsion between the fluorite layer and adjacent layers.[6,9]

While tunning CBM in compounds with the double fluorite layer is not straightforward,[10,11] we recently demonstrated a drastic CBM change by replacing the M cation in Bi_2MO_4Cl (M = Y, La, Bi),[10] comprising a triple fluorite Bi_2MO_4 slab. Bi_2YO_4Cl has the ideal structure (Fig. 1a), whereas Bi_2LaO_4Cl and Bi_3O_4Cl[10] contain broken Bi–O bonds, resulting in double and single zigzag chains, respectively, composed of BiO_3 units (Fig. S1†). The CBM shifts higher with Y → La → Bi due to the

[a]*Department of Energy and Hydrocarbon Chemistry, Graduate School of Engineering, Kyoto University, Kyoto 615-8510, Japan. E-mail: daichik@scl.kyoto-u.ac.jp; kage@scl.kyoto-u.ac.jp*

[b]*National Research Nuclear University MEPhI (Moscow Engineering Physics Institute), 31 Kashirskoye Shosse, Moscow 115409, Russia*

[c]*Department of Applied Quantum Physics and Nuclear Engineering, Kyushu University, Fukuoka 819-0395, Japan*

[d]*Department of Material Chemistry, Graduate School of Engineering, Kyoto University, Kyoto 615-8510, Japan*

[e]*Department of Applied Chemistry, Graduate School of Engineering, Osaka University, Osaka 565-0871, Japan*

[f]*Department for Solar Energy Materials and Technologies, Institute for Energy Technology, Kjeller, NO 2027, Norway. E-mail: smagul.karazhanov@ife.no*

† Electronic supplementary information (ESI) available: Reflectance spectra, refinement data. See DOI: https://doi.org/10.1039/d4sc02092h

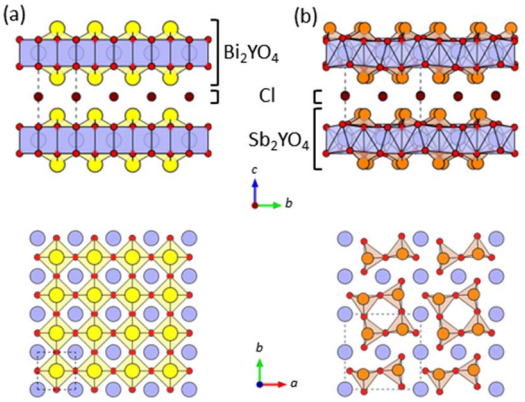

Fig. 1 The crystal structures of (a) Bi_2YO_4Cl[28] and (b) Sb_2YO_4Cl[29] with triple fluorite slabs, viewed along the [100] direction (top) and the [001] direction (bottom). Yellow, orange, blue, red, and brown spheres indicate Bi, Sb, Y, O and Cl atoms, respectively. Broken lines represent the unit cell. Bi/Sb–O bonds with negligible bond valence (<0.1) are not drawn (Table S5†).

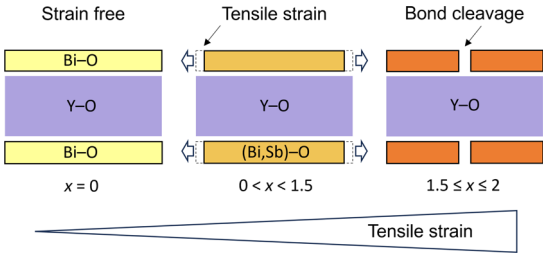

Fig. 2 Schematic illustration showing 'tensile strain' by Sb substitution in Bi_2YO_4Cl. With the Sb substitution of Bi, tensile strain is imposed from the inner YO_2 sublayer (blue) to the outer (Bi,Sb)O sublayer within the $(Bi,Sb)_2YO_4$ triple fluorite slab, eventually leading to a phase transition with bond-cleaved Sb_2YO_4Cl-type structure.

anti-bonding interaction allowed by breaking the mirror symmetry at the Bi site. However, the fundamental queries regarding the mechanism of the Bi–O bond cleavage and its exclusive occurrence in compounds with the triple-layer fluorite block remain unresolved.

From a broader perspective, manipulating the formation and cleavage of chemical bonds is generally important in solid-state chemistry since it often induces a variety of novel properties.[12–15] For example, in $SrCo_2(Ge_{1-x}P_x)_2$,[14] a ferromagnetic phase appears in the vicinity of the so-called collapse phase transition ($x \approx 0.5$). In $IrTe_2$, the chemical substitution of Pt causes the Ir–Ir bonds of the triangular lattice to break, resulting in superconductivity.[16] More recently, anion redox involving bond formation of an anion such as oxygen and sulfur has attracted much attention for the development of high-capacity battery materials.[17,18] In these examples, the underlying mechanism of the formation/breaking of chemical bonds in extended solids is attributed to the electron transfer between transition metal and the (molecular) anions, and hence they can be controlled by adjusting the relative energy of transition metal d states and anti-bonding states of molecular anions through, for example, intercalation, high pressure, and chemical substitutions.[12,14,16–21]

On the other hand, the mechanism and control of bond breaking in Bi_2MO_4Cl remain to be elucidated, but an interesting mechanism different from the above examples involving redox processes is expected. In this study, we newly synthesized an entire isovalent solid solution $Bi_{2-x}Sb_xYO_4Cl$ and investigated its phase transition behavior from the ideal Bi_2YO_4Cl structure to Sb_2YO_4Cl with isolated Sb_4O_8 rings (Fig. 1)[22,23] to elucidate the bond breaking process of the (Bi,Sb)–O square net. We found that upon substituting smaller Sb^{3+}, the expected lattice contraction is observed for $x < 0.6$, but further substitution leads to unexpected lattice expansion, ultimately inducing a transition to the Sb_2YO_4Cl phase at $x = 1.5$. Similar to the well-studied oxide thin films, where biaxial strain from a substrate affects and controls properties,[24–29] the structural instability, featured by lattice expansion ($0.6 < x < 1.5$), can be regarded as tensile strain from the middle YO_2 sublayer to outer (Bi,Sb)O sublayers in the triple fluorite slab (Fig. 2). With this concept, the crystal structures of Bi_2LaO_4Cl and Bi_3O_4Cl with zigzag chains[10] can also be reasonably explained. The variation in bandgap of $Bi_{2-x}Sb_xYO_4Cl$ corroborates with the lattice parameter evolution, with a minimum bandgap of 2.1 eV at around $x = 0.5$, suggesting the potential for enhanced catalytic activity at shorter wavelengths.

Results and discussion

Let us start by comparing the crystal structures of Bi_2YO_4Cl[28] and Sb_2YO_4Cl,[29] as shown in Fig. 1. Bi_2YO_4Cl is of tetragonal symmetry (space group: $P4/mmm$), with outer sublayers composed of corner-sharing BiO_4 square pyramids connected by eight-coordinate Y ions, forming a triple fluorite slab. These slabs stack along the c axis, with a Cl layer in between. In the case of Sb_2YO_4Cl, the outer sublayers are heavily distorted, yielding SbO_3 units that assemble into Sb_4O_8 ring.[29] This results in a $2a \times 2b \times c$ superstructure compared to Bi_2YO_4Cl (space group: $P42_12$).[28,29] Thus, Sb_2YO_4Cl manifests as a zero-dimensional (0D) system comprising isolated rings, differing from the one-dimensional (1D) zigzag chains in distorted Bi_3O_4Cl and Bi_2LaO_4Cl and the two-dimensional (2D) square net of ideal Bi_2YO_4Cl (Fig. S1†).[10]

Synchrotron powder X-ray diffraction (SPXRD) patterns of $Bi_{2-x}Sb_xYO_4Cl$ are presented in Fig. 3. For $x \leq 1.25$, all peaks can be indexed based on the ideal Bi_2YO_4Cl structure without superlattice peaks, except for small unidentified impurity peaks for $x = 0.2$ and $x \geq 0.8$. This suggests the successful formation of the solid solution with the ideal $P4/mmm$ structure. The absence of second harmonic generation (SHG) in $x = 0.7$–1.25 is consistent with the centrosymmetric structure. For all compositions, peaks are sharp, indicating high crystallinity of our samples. The local structure does not show any deviation from the average structure, as shown by the analysis of pair distribution function (PDF) for $0 \leq x \leq 1$ (Fig. S6 and Table S3†). For $x \geq 1.5$, the $2a \times 2b \times c$ superlattice peaks are observed, indicating a phase transition to the $P42_12$ structure (Fig. 3 and S2†). Energy dispersive X-ray (EDX) analysis showed that the Bi, Sb,

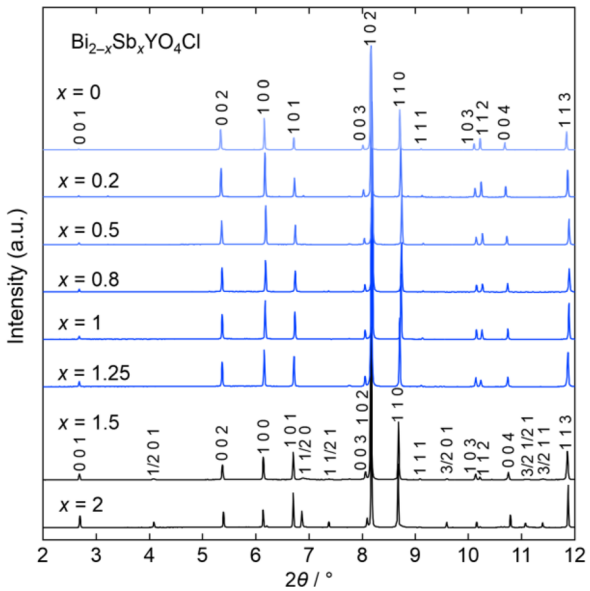

Fig. 3 Room temperature SPXRD patterns of $Bi_{2-x}Sb_xYO_4Cl$ ($0 \leq x \leq 2$). The samples with $x \leq 1.25$ are indexed with the *P*4/*mmm* space group (Bi_2YO_4Cl structure). Peaks are indexed based on the ideal tetragonal structure of Bi_2YO_4Cl. See Fig. S2† showing the absence of superlattice peaks for $x \leq 1.25$. The data was collected at a wavelength of $\lambda = 0.41946$ Å ($x \leq 1$) or 0.41362 Å ($1 < x \leq 2$).

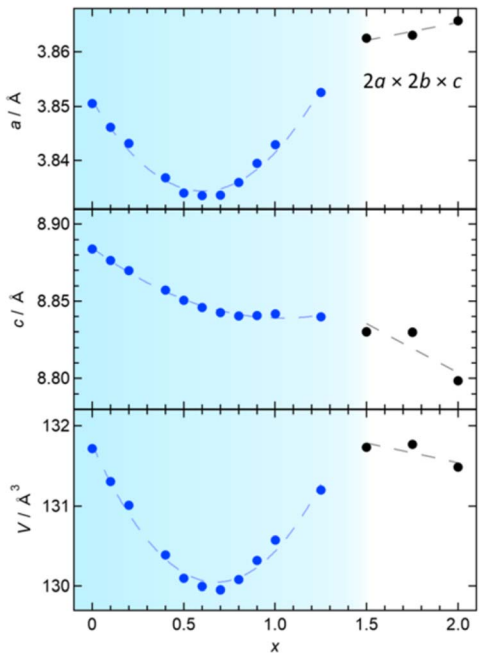

Fig. 4 The x dependence of the lattice parameters in $Bi_{2-x}Sb_xYO_4Cl$ ($0 \leq x \leq 2$): (top) a-axis, (middle) c-axis, and (bottom) volume. For $1.5 \leq x \leq 2$, the a-axis and volume are normalized to the ideal *P*4/*mmm* unit cell.

and Cl ratios in all samples closely match with the stoichiometry of the target compounds (Table S1†). The selected area electron diffraction (SAED) pattern of $BiSbYO_4Cl$ ($x = 1.0$) along the [001] direction shows no superlattice reflection, consistent with the *P*4/*mmm* structure (Fig. S3†).

The *P*4/*mmm* phase ($0 \leq x \leq 1.25$) has an anomaly in the x dependence of lattice constants, as shown in Fig. 4. Initially, both the a and c axes display a linear decrease with increasing x ($\leq$0.4), consistent with the variance in ionic radii between Sb^{3+} and Bi^{3+} (0.76 Å *vs.* 1.17 Å).[30] Upon further Sb-substitution, the a-axis decreases more slowly, reaching a minimum at $x = 0.6$ and then increases. At the same time, the c-axis departs from linear dependence and becomes nearly constant above $x = 0.7$. As a result, the volume change reaches a minimum around $x = 0.7$ and then increases up to $x = 1.25$. In the $P42_12$ region ($1.5 \leq x \leq 2$), the c-axis and (normalized) volume decrease as anticipated from the difference in ionic radii, while the normalized a-axis increases, continuing the trend observed in the later region of the Bi_2YO_4Cl structure.

To understand the unconventional evolution of lattice parameters, Rietveld refinement was conducted on SPXRD data in the range of $0 \leq x \leq 1.25$, assuming the ideal Bi_2YO_4Cl structure (*P*4/*mmm*),[10,28] where distribution of Bi and Sb atoms was randomized and their isotropic atomic displacement parameters (U_{iso}) were restricted to be equal. The refinement converged smoothly, yielding reasonable reliability factors, for example, GOF = 2.87%, R_p = 8.73%, and R_{wp} = 11.71% for $Bi_{1.3}Sb_{0.7}YO_4Cl$ (Fig. 5a and Table S2†). The results are summarized in Fig. S4,† with the refined parameters listed in Table S2.† No discernible deviations from the average crystal

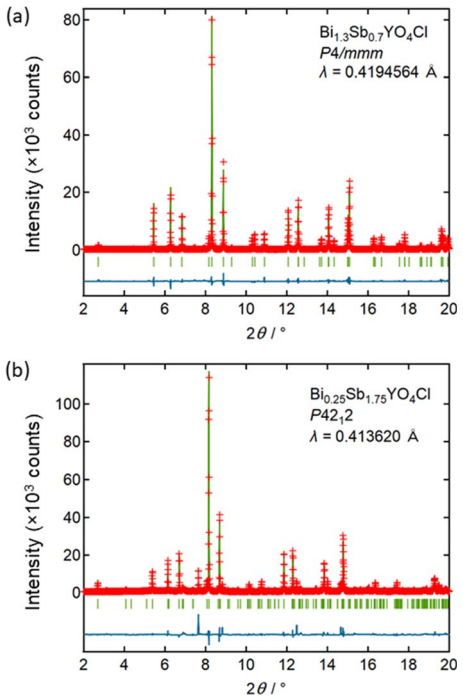

Fig. 5 The Rietveld refinement on SPXRD data of (a) $Bi_{1.3}Sb_{0.7}YO_4Cl$, assuming the Bi_2YO_4Cl (*P*4/*mmm*) model, and (b) $Bi_{0.25}Sb_{1.75}YO_4Cl$, assuming the Sb_2YO_4Cl ($P42_12$) model. The red markers, the green solid line, and the blue solid line represent observed, calculated and difference intensities, respectively. The green ticks indicate the calculated Bragg reflections.

structure were identified from pair-distribution function (PDF) analysis (Fig. S6 and Table S3†) and high-angle annular dark-field scanning transmission electron microscopy (HAADF-STEM) images (Fig. S3†). For $1.5 \leq x \leq 2$, Rietveld refinement was performed, assuming the Sb_2YO_4Cl structure ($P42_12$),[29] where similar restrictions on U_{iso} of randomly distributed Bi and Sb were applied. This also converged smoothly (Fig. 5b and Table S2†).

The information obtained from the structural refinement provides insight into the anomalous lattice evolution near the phase boundary and the mechanism behind the bond cleavage of the (Bi,Sb)O sublayer. A crucial observation is the gradual growth of lattice volume above $x = 0.7$ without a significant jump, even in close proximity to the phase boundary. This suggests an intimate relationship between lattice expansion for $0.5 < x < 1.5$ and (Bi,Sb)–O bond cleavage in the Sb_2YO_4Cl-type structure. Bond valence sum (BVS) calculations (Fig. 6b and c) reveal that Y^{3+} maintains nearly ideal values in the entire solid solution, while Sb^{3+} is fairly underbonded in the tetragonal structure ($x \leq 1.25$) but becomes closer to the ideal coordination in Sb_2YO_4Cl structure ($1.5 \leq x \leq 2$). This difference implies for the higher flexibility of Sb^{3+} coordination compared to Y^{3+}, allowing stretching of (Bi,Sb)–O prior to the phase transition. It possibly enhances the structural instability as clearly seen in the global instability index (GII), which is the summation of the deviation of BVS from the formal charge (Fig. 6d).

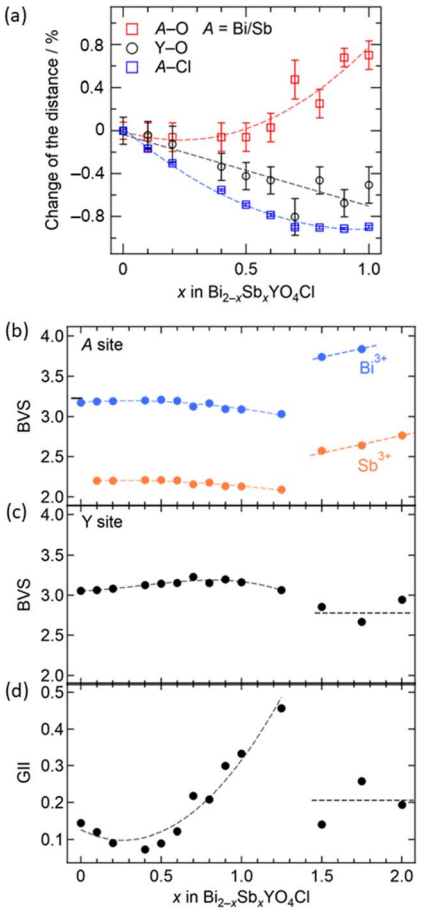

Fig. 6 (a) The x dependence ($0 \leq x \leq 1$) of A–O (red), A–Cl (blue) and Y–O (black) distances obtained from the Rietveld refinement of the $Bi_{2-x}Sb_xYO_4Cl$ solid solution (where A = Bi, Sb). The relative change with respect to $x = 0$ is shown. For A–Cl, error bars are within the markers. The x dependence of (b) the BVS of the A site assuming full occupation of Bi^{3+} (blue) and Sb^{3+} (orange) cations, and (c) the Y site, and (d) the global instability index (GII) for $0 \leq x \leq 2$. Dashed lines are guides for the eyes.

Combining these observations with the fact that Bi_2YO_4Cl is a stable structure, we propose that the substitution of smaller Sb^{3+} can lead to a mismatch between the outer (Bi,Sb)O and the inner YO_2 sublayer within the triple fluorite slab. This mismatch gives a tensile strain to the outer (Bi,Sb)O sublayer, which is exerted from the central YO_2 sublayer (Fig. 2). In the low substitution region ($x < 0.5$), the $(Bi,Sb)O_4$ pyramidal volume changes only slightly due to the increase of its height (Fig. S5†). However, as the tensile strain to the outer (Bi,Sb)O sublayer increases ($x > 0.5$), the $(Bi,Sb)O_4$ pyramid expands rapidly, enhancing the structural instability (Fig. 6d and S5†).

The manipulation of chemical bonds can lead to unique properties including unconventional superconductivity of $BaNi_2(Ge_{1-x}P_x)_2$ and $BaTi_2Pn_2O$ (Pn = As, Sb)[13,20] in the vicinity of P–P/Pn–Pn bond breaking and in high-energy-density cathode materials (*e.g.*, $La_{1.2}Sr_{1.8}Mn_2O_{7-\delta}F_2$) involving anion redox.[17,31,32] In these cases, the bond breaking involves redox of transitions metal and anions (*e.g.*, $2Pn^{3-} \Leftrightarrow (Pn\text{–}Pn)^{4-} + 2e^-$) and thus the relative energy between d orbitals of transition metals and p orbitals of (molecular) anions, which is controlled, for example, by intercalation, application of pressure and chemical substitution. In contrast, in the present study, the formation/breaking of chemical bonds in the $(Bi,Sb)O_2$ square net occurs free of redox processes and originates from the biaxial strain exerted from the inner Y sublayer. The strain concept is ubiquitous in thin film research: physical properties can be controlled by applying compressive or tensile strain from the substrate.[24–29] Strain effects in compounds with alternating layers are commonly addressed to alter physical properties,[33,34] but the occurrence of drastic bond formation/cleavage is, to the best of our knowledge, unknown.

The strain concept introduced above provides a plausible explanation of the Bi_2MO_4Cl structures, wherein only M = La and Bi induce bond breaking, resulting in 1D zigzag chains, unlike when M = Y.[10] In the case of Bi_2MO_4Cl, the M cations in the central MO_2 sublayer vary while maintaining the outer BiO sublayer.[10] By substituting M from Y^{3+} (1.02 Å) to the larger La^{3+} (1.16 Å) or Bi^{3+} (1.17 Å)[30] (Fig. 7), the outer BiO sublayer is subject to tensile strain, which causes the Bi–O bonds to break, forming 1D single or double zigzag chains. We anticipate that this strain effect can occur in compounds with $n \geq 3$ fluorite layers that are yet to be developed. Hence, this approach can be a useful strategy in the quest for novel photocatalysts and other functions. Indeed, the presence of corrugated sextuple fluorite blocks ($n = 6$), with partial inclusion of the rock-salt 1D block, can also be considered to appear as a consequence of strain

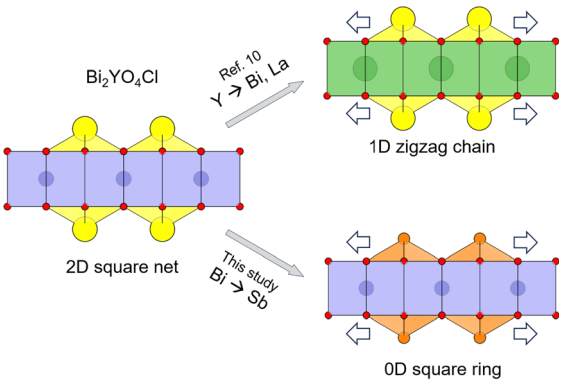

Fig. 7 Scheme of manipulating Bi_2YO_4Cl structure by substitution-induced tensile strain from the inner sublayer to the outer sublayer within the Bi_2YO_4 triple-fluorite slab. (top) Y-site substitution of the inner sublayer with larger Bi or La cations (Bi_2LaO_4Cl and Bi_3O_4Cl) transforms the outer BiO sublayer (2D square net) into 1D zigzag chains.[10] (bottom) In this study, Bi-site substitution of the outer sublayer to smaller Sb cation ($Bi_{2-x}Sb_xYO_4Cl$) transforms the outer sublayer into 0D square rings for $x \geq 1.5$. Yellow, orange, blue, green, and red spheres indicate Bi, Sb, Y, La, and O atoms, respectively.

between outer and inner layers of the hypothetical ideal $n = 6$ fluorite structure.[35]

To understand the impact of Sb substitution and strain effect on the electronic structures, we measured diffuse reflectance spectra (Fig. S7†). Tauc plots revealed that the bandgap reduces from 2.5 eV for $x = 0$ to 2.1 eV for $x = 0.5$ (Fig. 8a). With a further increase in Sb, however, the bandgap expands to 2.35 eV for $x = 1$, correlating with the anomalous change in lattice constants. This change is consistent with the observed coloration of the samples: yellow for $x = 0$ and 1, and bright orange for $x = 0.5$ (Fig. S8†). Fig. 8b shows the positions of the VBM and CBM, determined from absorption spectra and photoelectron yield spectroscopy (PYS) measurements (Fig. S9†). The VBM shifts upward from 2.07 V ($x = 0$) to 1.7 V ($x = 0.5$) and then downward to 1.95 V ($x = 1$), whereas the CBM value, obtained by subtracting the bandgap from the ionization energy, remains almost constant. Hence, the change in VBM predominantly accounts for the narrowed bandgap. It is notable that the bandgaps for $0.2 \leq x \leq 0.8$ are among the smallest of oxychloride photocatalysts, with the exception of $Bi_{2.8}Y_{0.2}O_4Cl$ with 2.0 eV.[36–38]

In addition, we conducted DFT calculations for Bi_2YO_4Cl and $Bi_{1.5}Sb_{0.5}YO_4Cl$ (see Fig. S10 and Table S4† for details). As shown in Fig. 9a, it is evident that the VBM of Bi_2YO_4Cl primarily comprises O-2p orbitals, with a certain contribution from Bi-6s/6p orbitals, indicating that the VBM is formed by the lone pair interaction of Bi.[8,11,39,40] In contrast, in $Bi_{1.5}Sb_{0.5}YO_4Cl$ (Fig. 9b), the VBM contribution mainly stems from the Sb-5s/5p orbitals rather than Bi orbitals. Furthermore, the bonding orbitals between Sb-5s and O-2p (around −8 eV) are higher than those of the Bi-6s states (−9–12 eV), likely due to relativistic effects,[41] leading to higher energy levels of atomic Sb-5s orbitals compared to Bi-6s orbitals.[41,42] Therefore, the energy rise of VBM upon minor Sb substitution can be attributed to the closer

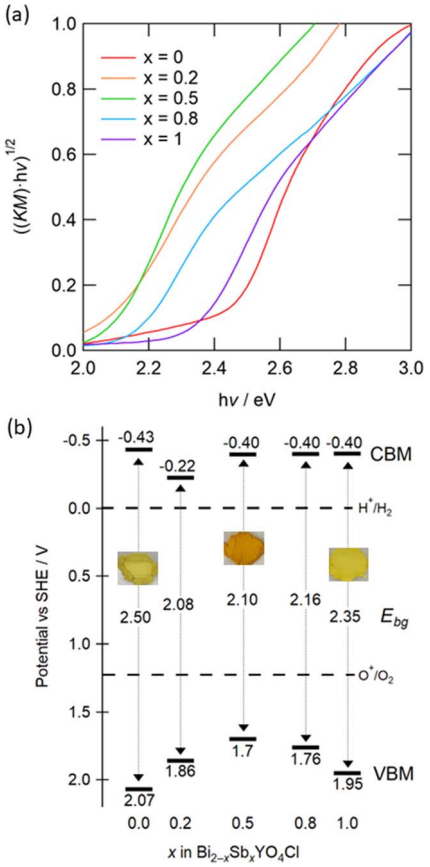

Fig. 8 (a) Tauc plots of $Bi_{2-x}Sb_xYO_4Cl$ ($0 \leq x \leq 1$) obtained from UV-visible diffuse reflectance spectra. Corresponding reflectance spectra are shown in Fig. S7.† (b) Schematic band diagrams estimated from the bandgap and the lowest ionization energy. Values in the middle between the CBM and the VBM represent the bandgap (E_{bg}). The standard electrode potential is converted to −([absolute electron potential in a vacuum] + 4.44 V) (*vs.* SHE at the isoelectric point). Embedded photos demonstrate the colour of samples with $x = 0$, 0.5, 1 (see Fig. S8† for details).

energy levels between Sb-5s and O-2p orbitals, enabling stronger lone pair interactions (Fig. 9a).

Interestingly, the bandgaps of Sb-substituted Bi_2YO_4Cl ($x \sim 0.5$) are remarkably narrow, even when compared to Sb-based oxychlorides (*e.g.*, 3.5 eV for $Sb_4O_5Cl_2$,[43] and 4.0 eV for SbOCl[42]). In addition, the downshift of VBM occurs at $x > 0.5$ despite the increase in the Sb ratio (Fig. 8b), an observation that cannot be solely explained by simply considering the higher atomic levels of Sb-5s (*vs.* Bi-6s). In general, the stereochemical activity of LPEs can be enhanced when the lone-pair containing cations (*e.g.*, Bi^{3+}, Sb^{3+}) occupy a larger space.[44–46] Given that Sb^{3+} is relatively small for the Bi^{3+} site,[30] the lone pair interaction of Sb in the lower x region may be enhanced. However, further substitution beyond $x = 0.5$ elongates the (Bi,Sb)–O bonds (Fig. 6a), weakens the Sb–O lone pair interaction and lowers the VBM level. This scenario resembles that of perovskite $CsSnBr_3$, where the off-centring is suppressed by competition with octahedral tilting distortions upon cooling.[46] In our case, competition with bond-breaking distortion may elongate the Sb–O distance and hence weaken the Sb–O lone pair interactions.

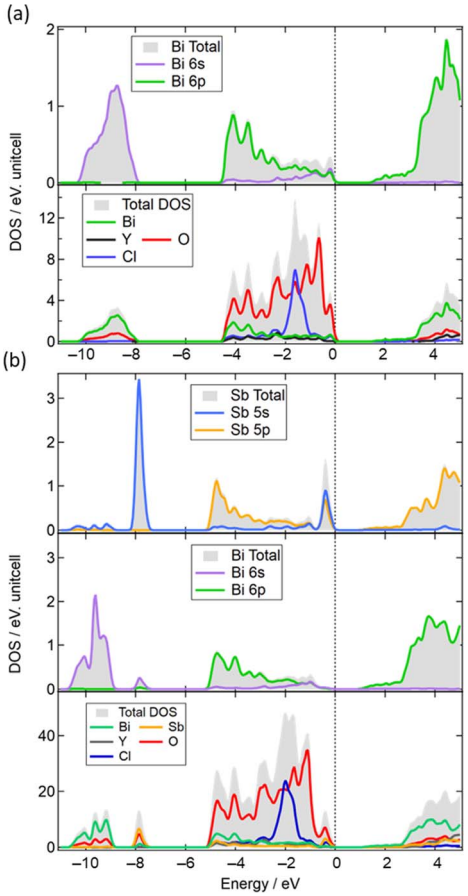

Fig. 9 (a) Density of states (DOS) of Bi_2YO_4Cl and partial DOS (PDOS) for Bi 6s and Bi 6p states. (b) DOS of $Bi_{1.5}Sb_{0.5}YO_4Cl$ and PDOS for Sb and Bi.

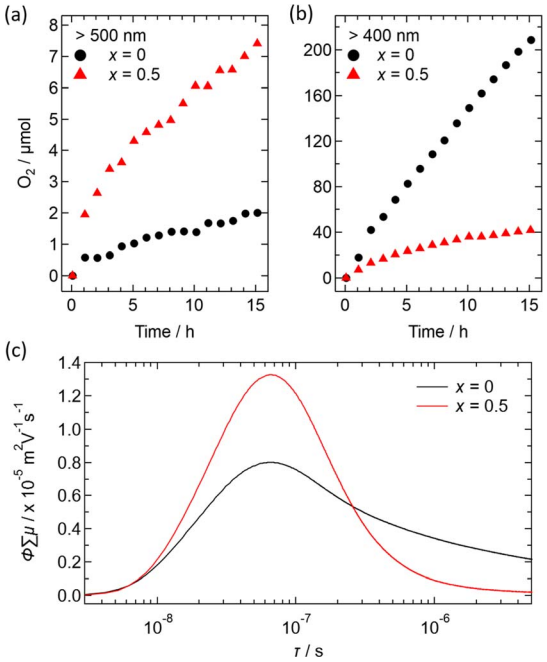

Fig. 10 Time course of O_2 production over Bi_2YO_4Cl ($x = 0$) and $Bi_{1.5}Sb_{0.5}YO_4Cl$ ($x = 0.5$) from water, containing 4 mM of $AgNO_3$ as an Ag^+ electron acceptor under the visible light irradiation with wavelengths (a) >500 nm and (b) >400 nm, produced by Xe lamp with L52 and L42 cutoff filters respectively. Photocatalysts had been initially loaded with 5 wt% of Ir as cocatalyst. (c) Transient conductivities of Bi_2YO_4Cl ($x = 0$) and $Bi_{1.5}Sb_{0.5}YO_4Cl$ ($x = 0.5$) upon 355 nm laser excitation. The vertical axis represents the product of the quantum efficiency φ and the sum of photogenerated carrier mobilities $\sum\mu$. The horizontal axis represents the lifetime in logarithmic scale.

Fig. 10 illustrates preliminary photocatalytic results for O_2 evolution from water using Ir-loaded $Bi_{2-x}Sb_xYO_4Cl$ ($x = 0$ and 0.5), with $AgNO_3$ as a sacrificial reagent. When irradiated with light longer than 500 nm, $Bi_{1.5}Sb_{0.5}YO_4Cl$ showed approximately 5 times higher activity than parent Bi_2YO_4Cl (Fig. 10a and b). This increase in activity indicates that the Sb-substituted sample can utilize a wider range of light wavelengths due to its narrower bandgap. However, the oxygen evolution is not very high, indicating the need for surface improvements. When exposed to the light with $\lambda > 400$ nm, the activity is enhanced but remains lower than that of pristine Bi_2YO_4Cl.

The transient conductivity measurements revealed an improved mobility of photogenerated carries for $x = 0.5$, in comparison to $x = 0$ (Fig. 10c). This enhancement could be ascribed to a shorter (Bi,Sb)–O distance, leading to increased band dispersion. On the other hand, the $x = 0.5$ sample exhibits faster decay of the photoconductivity, suggesting that Sb-substitution increases the number of defects acting as recombination centers. Addressing this issue may involve adjusting the synthesis conditions and the choice of cocatalyst, as demonstrated in other materials,[47,48] though this is beyond the scope of our current study and remains a future challenge.

Conclusions

We have successfully synthesized the entire solid solution $Bi_{2-x}Sb_xYO_4Cl$ containing the triple fluorite layer, unveiling a clue of (Bi,Sb)–O bond breaking, a phenomenon that never occurs in compounds with conventional double fluorite layers. A small Sb substitution ($x \leq 0.5$) induces the anticipated lattice contraction, but further substitutions lead to lattice expansion, finally causing a phase transition to the Sb_2YO_4Cl-type structure with 0D $(Bi,Sb)_4O_8$ rings. The structural instability observed in the high x region, characterized by Sb–O underbonding (which eventually leads to bond cleavage at $x \geq 1.5$), can be rationalized as a result of biaxial tensile strain exerted from the central YO_2 sublayer to the outer (Bi,Sb)O sublayers within the triple fluorite block. This is similar to a strategy widely used in thin film studies, *i.e.*, strain from a substrate, and can also reasonably explain the structure evolution to Bi_2MO_4Cl (M = Bi, La) with 1D zigzag chains. While the VBM remained uncontrolled in Bi_2MO_4Cl, Sb substitution in $Bi_{2-x}Sb_xYO_4Cl$ varies the VBM alongside a nonlinear change in lattice constants, narrowing the bandgap from 2.5 eV ($x = 0$) to 2.1 eV ($x = 0.5$). Our findings highlight the potential of fluorite structures comprising triple or more layers for bandgap engineering by introducing biaxial strain from the inner slab to the outer slab, or *vice versa*. This unique situation is absent in layered perovskites, which have

been extensively studied as functional materials, and this study encourages the search for materials with thicker fluorite layers toward realizing new functions in a variety of fields.

Experimental

Synthesis and characterization

A series of $Bi_{2-x}Sb_xYO_4Cl$ solid solutions were obtained using the flux method or by solid-state reaction (SSR). For the SSR synthesis, powders of BiOCl (Wako, 95.0+%), Sb_2O_3 (Wako, 99.99%), Bi_2O_3 (Wako, 99.99%), and Y_2O_3 (Wako, 99.99%) were mixed in stoichiometric ratio, thoroughly grinded, and pelletized. Then, the pellet was loaded in an alumina tube, which was placed in a silica tube and vacuum-sealed. The pellets were heated twice to 800 °C with intermediate grinding. For flux synthesis, CsCl (Wako, 99.0%) was chosen as flux following the previous studies of oxyhalide photocatalysts.[10,29] 19 times CsCl was added to the stoichiometric mixture of other starting materials. After 20 hours of reaction at 800 °C, the products were carefully washed with water and dried overnight at 100 °C followed by heating in air at 400 °C for 1 hour. SPXRD and SHG data were obtained from samples synthesized by solid state reaction, while photocatalytic measurements were performed with samples obtained by flux synthesis.

Synchrotron powder XRD (SPXRD) patterns were collected at the BL02B2 beamline in SPring-8, Japan ($\lambda = 0.41327(1)$ Å) and were analysed using Jana2006.[49] High-angle annular dark-field scanning transmission electron microscopy images (HAADF-STEM) and selected area diffraction pattern (SAED) were collected using a JEM-ARM200CF, JEOL microscope operating at an accelerating voltage of 80 kV. UV-vis spectrophotometer (UV-2600, Shimadzu) was used to measure reflectance spectra, then the data were transformed to Kubelka–Munk, $F(R)$, function.[50] The band gaps were obtained by Tauc plots, where $(F(R) \times h\nu)^n$ is plotted against energy $h\nu$ (eV) assuming $n = 0.5$ for a indirect bandgap transition.[51,52] The ionization energy was measured by photoelectron yield spectroscopy (PYS; BIP-KV201, Bunkoukeiki) in vacuum ($<5 \times 10^{-2}$ Pa). The experimental pair distribution function (PDF), $G(r)$, were obtained from the total scattering structure function $S(Q)$ in variable Q ranges measured at the BL13XU beamline in SPring-8, Japan ($\lambda = 0.334614(1)$ Å). Fourier transformation was carried out using the PDFgetX3 program.[53] Further refinement was performed using PDFfit2 software.[54]

Optical second harmonic generation (SHG) measurements were performed at room temperature. As the light source, a pulsed Nd:YAG laser with a wavelength of 1064 nm was used. Pulse duration was 25 ps with repetition frequency of 10 Hz. A photomultiplier tube with a 532 nm narrow band-pass filter was used to detect the SHG light from the sample.

Time-resolved microwave conductivity (TRMC) measurements were conducted on samples synthesized *via* the flux method under ambient conditions using a third harmonic generator (THG; 355 nm).[55] A Nd:YAG laser (Continuum Inc., Surelite II) emitting pulses with a duration of 5–8 ns pulse duration and a frequency of 10 Hz served as the excitation source (4.6×10^{15} photons per cm^2 per pulse). An X-band microwave with a frequency of ~9.1 GHz acted as the probe. The transient photoconductivity $\Delta\sigma$ was calculated using the formula $\Delta P_r/A \times P_r$, where ΔP_r, A, and P_r represent the transient power change of the reflected microwave power, the sensitivity factor, and the reflected microwave power, respectively. The transient photoconductivity $\Delta\sigma$ was then converted to the product of the quantum yield and the sum of charge carrier mobilities, $\sum\mu = \mu_+ + \mu_-$, using the formula $\varphi \times \sum\mu = \Delta\sigma \times (e \times I_0 \times F_{light})^{-1}$, where e and F_{light} denote the unit charge of a single electron and a correction (or filling) factor, respectively.

DFT calculations

The electronic structures of Bi_2YO_4Cl and $Bi_{1.5}Sb_{0.5}YO_4Cl$ were calculated using the VASP Package.[56,57] For $Bi_{1.5}Sb_{0.5}YO_4Cl$, a $2 \times 2 \times 1$ superlattice was constructed, wherein Sb and Bi atoms were alternatively positioned in the triple fluorite layer (Fig. S10†) The exchange and correlation energies were evaluated within the generalized gradient approximation (GGA) of density functional theory (DFT), as proposed by Perdew, Burke, and Ernzerhof (PBE).[58,59] The supercell of $Bi_{1.5}Sb_{0.5}O_4Cl$ (Fig. S10†) is generated using SHRY.[60] The electronic states were expanded by using a plane-wave basis set with a cutoff energy of 800 eV. The $12 \times 12 \times 6$ k-points were used. Geometry optimization was performed before calculating the electronic structures using the Broyden–Fletcher–Goldfarb–Shanno (BFGS) algorithm.[61–64] The calculated lattice parameters reasonably agree with the lattice parameters obtained from diffraction experiments (Table S4†).

Photocatalytic reaction

In prior to the photocatalytic measurements, Bi_2YO_4Cl and $Bi_{1.5}Sb_{0.5}YO_4Cl$ powder samples were impregnated with Ir as cocatalyst. In this process, a photocatalyst was mixed with certain amount of $Na_2IrCl_6 \cdot 6H_2O$ (Strem Chemicals) water solution, corresponding to 0.5 wt% of Ir (assuming, for simplicity, a metallic state of cocatalyst). After that, the mixture was heated on a hot water bath until dry. Then, the result powder was heated under Ar flow at 450 °C for 30 min.

Photocatalytic reactions were performed in a closed gas-circulation system using a Pyrex reaction vessel, which had been degassed and purged with Ar gas before measurements. The evolved gases were analysed using online gas chromatography (GC3210, GL Sciences, Ar carrier gas). For photocatalytic O_2 evolution, the $Bi_{2-x}Sb_xYO_4Cl$ photocatalyst (0.1 g) preliminary loaded with Ir (0.5 wt%) as cocatalyst was suspended in a 250 ml of 4 mM aqueous solution of $AgNO_3$ (Wako, 99.9%). A Xe lamp (LAMP HOUSE R300-3J, Eagle engineering, 300 W) equipped with a cold mirror (CM-1, Kenko) and a cut-off filter was used as a light source. For irradiation of $\lambda > 400$ nm and $\lambda > 500$ nm light, cut-off filters L-42 and L-52 (HOYA Corporation) were used, respectively.

Data availability

ICSD 2343994–2344007 contain the supplementary crystallographic data for this paper.

Author contributions

A. G., D. K., H. K., S. K., designed the project. A. G., N. K. synthesized the samples. D. K. performed DFT calculations. A. G., H. U., D. K. collected and analysed SPXRD data and PDF data. R. A., D. K. carried out TEM measurements. K. F. carried out SHG measurement. A. G. performed the measurement of physical properties. H. S., O. T., R. A. contributed to the measurement of photocatalytic properties. A. S. and H. S. performed the TRMC measurements. A. G., D. K., H. K. wrote the manuscript, with comments from other authors.

Conflicts of interest

The authors declare no competing financial interest.

Acknowledgements

This work was supported by JST PRESTO (JPMJPR21A5), JSPS Core-to-Core Program (A) Advanced Research Networks (JPJSCCA20200004), the Grant-in-Aid for Scientific Research on Innovative Areas "Mixed Anion" project (16H06438, 16H06439), JSPS KAKENHI (JP21K20556, JP20H00398, JP22H04914, JP23H04860), and CREST (JPMJCR1421). TEM measurement was supported by "Advanced Research Infrastructure for Materials and Nanotechnology in Japan (ARIM)" of the Ministry of Education, Culture, Sports, Science and Technology (MEXT) (Proposal No. JPMXP1222KU0040 and JPMXP1223KU0023). The SPXRD experiments were performed at the BL02B2 of SPring-8 (Proposal No. 2022A1081 and 2022B1964). AG and SZK have received funding from the Project 309827 within the International Partnerships for Excellent Education, Research and Innovation Program of the Research Council of Norway. Special recommendation: COOL LONGBOAT project.

References

1 H. Kunioku, M. Higashi and R. Abe, *Sci. Rep.*, 2016, **6**, 32664.
2 T. Takata, C. Pan and K. Domen, *Sci. Technol. Adv. Mater.*, 2015, **16**, 33506.
3 K. Maeda, F. Takeiri, G. Kobayashi, S. Matsuishi, H. Ogino, S. Ida, T. Mori, Y. Uchimoto, S. Tanabe, T. Hasegawa, N. Imanaka and H. Kageyama, *Bull. Chem. Soc. Jpn.*, 2022, **95**, 26–37.
4 J. Cui, C. Li and F. Zhang, *ChemSusChem*, 2019, **12**, 1872–1888.
5 H. Suzuki, H. Kunioku, M. Higashi, O. Tomita, D. Kato, H. Kageyama and R. Abe, *Chem. Mater.*, 2018, **30**, 5862–5869.
6 D. Kato, K. Hongo, R. Maezono, M. Higashi, H. Kunioku, M. Yabuuchi, H. Suzuki, H. Okajima, C. Zhong, K. Nakano, R. Abe and H. Kageyama, *J. Am. Chem. Soc.*, 2017, **139**, 18725–18731.
7 H. Fujito, H. Kunioku, D. Kato, H. Suzuki, M. Higashi, H. Kageyama and R. Abe, *J. Am. Chem. Soc.*, 2016, **138**, 2082–2085.
8 H. Kunioku, M. Higashi, O. Tomita, M. Yabuuchi, D. Kato, H. Fujito, H. Kageyama and R. Abe, *J. Mater. Chem. A*, 2018, **6**, 3100–3107.
9 D. Kato, R. Abe and H. Kageyama, *J. Mater. Chem. A*, 2019, **7**, 19846–19851.
10 A. Nakada, D. Kato, R. Nelson, H. Takahira, M. Yabuuchi, M. Higashi, H. Suzuki, M. Kirsanova, N. Kakudou, C. Tassel, T. Yamamoto, C. M. Brown, R. Dronskowski, A. Saeki, A. Abakumov, H. Kageyama and R. Abe, *J. Am. Chem. Soc.*, 2021, **143**, 2491–2499.
11 K. Ogawa, H. Suzuki, A. Walsh and R. Abe, *Chem. Mater.*, 2023, **35**, 5532–5540.
12 K. Kudo, H. Ishii, M. Takasuga, K. Iba, S. Nakano, J. Kim, A. Fujiwara and M. Nohara, *J. Phys. Soc. Jpn.*, 2013, **82**, 2–5.
13 D. Hirai, F. Von Rohr and R. J. Cava, *Phys. Rev. B: Condens. Matter Mater. Phys.*, 2012, **86**, 100505.
14 S. Jia, P. Jiramongkolchai, M. R. Suchomel, B. H. Toby, J. G. Checkelsky, N. P. Ong and R. J. Cava, *Nat. Phys.*, 2011, **7**, 207–210.
15 H. Yamamoto, T. Ogata, Y. Sakai and M. Azuma, *Inorg. Chem.*, 2019, **58**, 2755–2760.
16 S. Pyon, K. Kudo and M. Nohara, *J. Phys. Soc. Jpn.*, 2012, **81**, 053701.
17 H. Miki, K. Yamamoto, H. Nakaki, T. Yoshinari, K. Nakanishi, S. Nakanishi, H. Iba, J. Miyawaki, Y. Harada, A. Kuwabara, Y. Wang, T. Watanabe, T. Matsunaga, K. Maeda, H. Kageyama and Y. Uchimoto, *J. Am. Chem. Soc.*, 2024, **146**, 3844–3853.
18 J. J. Zak, S. S. Kim, F. A. L. Laskowski and K. A. See, *J. Am. Chem. Soc.*, 2022, **144**, 10119–10132.
19 S. Jia, A. J. Williams, P. W. Stephens and R. J. Cava, *Phys. Rev. B: Condens. Matter Mater. Phys.*, 2009, **80**, 165107.
20 T. Yamamoto, T. Yajima, Z. Li, T. Kawakami, K. Nakano, T. Tohyama, T. Yagi, Y. Kobayashi and H. Kageyama, *Inorg. Chem.*, 2021, **60**, 2228–2233.
21 R. Hoffmann, *Angew. Chem., Int. Ed. Engl.*, 1987, **26**, 846–878.
22 M. Schmidt, M. Oppermann, H. Hennig, C. Henn, R. W. Gmelin, E. Soeger and N. Binnewies, *Z. Anorg. Allg. Chem.*, 2000, **626**, 125–135.
23 R. J. C. Locke, F. C. Goerigk, M. J. Schäfer, H. A. Höppe and T. Schleid, *RSC Adv.*, 2022, **12**, 640–647.
24 J. P. Locquet, J. Perret, J. Fompeyrine, E. Mächler, J. W. Seo and G. Van Tendeloo, *Nature*, 1998, **394**, 453–456.
25 Y. Konishi, Z. Fang, M. Izumi, T. Manako, M. Kasai, H. Kuwahara, M. Kawasaki, K. Terakura and Y. Tokura, *J. Phys. Soc. Jpn.*, 1999, **68**, 3790–3793.
26 K. J. Choi, M. Biegalski, Y. L. Li, A. Sharan, J. Schubert, R. Uecker, P. Reiche, Y. B. Chen, X. Q. Pan, V. Gopalan, L. Q. Che, D. C. Schlom and C. B. Eom, *Science*, 2004, **306**, 1005–1009.
27 J. H. Lee, L. Fang, E. Vlahos, X. Ke, Y. W. Jung, L. F. Kourkoutis, J. W. Kim, P. J. Ryan, T. Heeg, M. Roeckerath, V. Goian, M. Bernhagen, R. Uecker, P. C. Hammel, K. M. Rabe, S. Kamba, J. Schubert, J. W. Freeland, D. A. Muller, C. J. Fennie, P. Schiffer, V. Gopalan, E. Johnston-Halperin and D. G. Schlom, *Nature*, 2010, **466**, 954–958.

28 T. Yamamoto, A. Chikamatsu, S. Kitagawa, N. Izumo, S. Yamashita, H. Takatsu, M. Ochi, T. Maruyama, M. Namba, W. Sun, T. Nakashima, F. Takeiri, K. Fujii, M. Yashima, Y. Sugisawa, M. Sano, Y. Hirose, D. Sekiba, C. M. Brown, T. Honda, K. Ikeda, T. Otomo, K. Kuroki, K. Ishida, T. Mori, K. Kimoto, T. Hasegawa and H. Kageyama, *Nat. Commun.*, 2020, **11**, 5923.
29 M. Namba, H. Takatsu, R. Mikita, Y. Sijia, K. Murayama, H. B. Li, R. Terada, C. Tassel, H. Ubukata, M. Ochi, R. Saez-Puche, E. P. Latasa, N. Ishimatsu, D. Shiga, H. Kumigashira, K. Kinjo, S. Kitagawa, K. Ishida, T. Terashima, K. Fujita, T. Mashiko, K. Yanagisawa, K. Kimoto and H. Kageyama, *J. Am. Chem. Soc.*, 2023, **145**, 21807–21816.
30 R. D. Shannon, *Acta Crystallogr.*, 1976, **32**, 751–767.
31 C. J. Hansen, J. J. Zak, A. J. Martinolich, J. S. Ko, N. H. Bashian, F. Kaboudvand, A. Van Der Ven, B. C. Melot, J. Nelson Weker and K. A. See, *J. Am. Chem. Soc.*, 2020, **142**, 6737–6749.
32 G. Assat and J. M. Tarascon, *Nat. Energy*, 2018, **3**, 373–386.
33 I. D. Brown, *Phys. C*, 1990, **169**, 105–106.
34 G. H. Kwei, P. C. Canfield, Z. Fisk, J. D. Thompson and R. B. Von Dreele, *Phys. C*, 1991, **176**, 57–63.
35 D. Kato, O. Tomita, R. Nelson, M. A. Kirsanova, R. Dronskowski, H. Suzuki, C. Zhong, C. Tassel, K. Ishida, Y. Matsuzaki, C. M. Brown, K. Fujita, K. Fujii, M. Yashima, Y. Kobayashi, A. Saeki, I. Oikawa, H. Takamura, R. Abe, H. Kageyama, T. E. Gorelik and A. M. Abakumov, *Adv. Funct. Mater.*, 2022, **32**, 2204112.
36 Y. Jiang, Y. Mi, C. Li, W. Fang, X. Li, X. Zeng, Y. Liu and W. Shangguan, *J. Alloys Compd.*, 2021, **884**, 161036.
37 C. Zhao, L. Sun, Y. Xu, B. Dong, Y. Luo, J. Li, J. Chen and Z. Zhang, *Chem.–Eur. J.*, 2022, **28**, 202202004.
38 K. Ogawa, R. Abe and A. Walsh, *J. Am. Chem. Soc.*, 2024, **146**, 5806–5810.
39 C. Zhong, D. Kato, K. Ogawa, C. Tassel, F. Izumi, H. Suzuki, S. Kawaguchi, T. Saito, A. Saeki, R. Abe and H. Kageyama, *Inorg. Chem.*, 2021, **60**, 15667–15674.
40 R. Kuriki, T. Ichibha, K. Hongo, D. Lu, R. Maezono, H. Kageyama, O. Ishitani, K. Oka and K. Maeda, *J. Am. Chem. Soc.*, 2018, **140**, 6648–6655.
41 A. Walsh, D. J. Payne, R. G. Egdell and G. W. Watson, *Chem. Soc. Rev.*, 2011, **40**, 4455–4463.
42 Z. Ran, X. Wang, Y. Li, D. Yang, X.-G. Zhao, K. Biswas, D. J. Singh and L. Zhang, *npj Comput. Mater.*, 2018, **4**, 14.
43 L. Yang, J. Huang, L. Cao, L. Shi, Q. Yu, X. Kong and Y. Jie, *Sci. Rep.*, 2016, **6**, 27765.
44 X. Li, Y. Guan, X. Li and Y. Fu, *J. Am. Chem. Soc.*, 2022, **144**, 18030–18042.
45 U. Dang, W. Zaheer, W. Zhou, A. Kandel, M. Orr, R. W. Schwenz, G. Laurita, S. Banerjee and R. T. MacAluso, *Chem. Mater.*, 2020, **32**, 7404–7412.
46 D. H. Fabini, G. Laurita, J. S. Bechtel, C. C. Stoumpos, H. A. Evans, A. G. Kontos, Y. S. Raptis, P. Falaras, A. Van Der Ven, M. G. Kanatzidis and R. Seshadri, *J. Am. Chem. Soc.*, 2016, **138**, 11820–11832.
47 K. Ogawa, A. Nakada, H. Suzuki, O. Tomita, M. Higashi, A. Saeki, H. Kageyama and R. Abe, *ACS Appl. Mater. Interfaces*, 2019, **11**, 5642–5650.
48 J. Yu, S. Chang, L. Shi and X. Xu, *ACS Catal.*, 2023, **13**, 3854–3863.
49 V. Petricek, L. Palatinus, J. Plasil and M. Dusek, *Z. Kristallogr.*, 2023, **238**, 271–282.
50 E. L. Simmons, *Appl. Opt.*, 1976, **15**, 951–954.
51 P. Makuła, M. Pacia and W. Macyk, *J. Phys. Chem. Lett.*, 2018, **9**, 6814–6817.
52 A. E. Morales, *Rev. Mex. Fis.*, 2007, **53**, 18–22.
53 P. Juhás, T. Davis, C. L. Farrow and S. J. L. Billinge, *J. Appl. Crystallogr.*, 2013, **46**, 560–566.
54 C. L. Farrow, P. Juhas, J. W. Liu, D. Bryndin, E. S. Boin, J. Bloch, T. Proffen and S. J. L. Billinge, *J. Phys.: Condens. Matter*, 2007, **19**, 335219.
55 A. Saeki, *Polym. J.*, 2020, **52**, 1307–1321.
56 G. Kresse and J. Hafner, *J. Phys.: Condens.Matter*, 1994, **6**, 8245–8257.
57 G. Kresse and D. Joubert, *Phys. Rev. B: Condens. Matter Mater. Phys.*, 1999, **59**, 1758–1774.
58 J. P. Perdew, K. Burke and M. Ernzerhof, *Phys. Rev. Lett.*, 1996, **77**, 3865–3868.
59 J. P. Perdew, A. Ruzsinszky, G. I. Csonka, O. A. Vydrov, G. E. Scuseria, L. A. Constantin, X. Zhou and K. Burke, *Phys. Rev. Lett.*, 2008, **100**, 136406.
60 G. I. Prayogo, A. Tirelli, K. Utimula, K. Hongo, R. Maezono and K. Nakano, *J. Chem. Inf. Model.*, 2022, **62**, 2909–2915.
61 D. Goldfarb, *Math. Comput.*, 1970, **24**, 23–26.
62 C. G. Broyden, *IMA J. Appl. Math.*, 1970, **6**, 76–90.
63 R. Fletcher, *Comput. J.*, 1970, **13**, 317–322.
64 D. F. Shanno, *Math. Comput.*, 1970, **24**, 647–656.